Boundary node Petrov-Galerkin method in solids mechanics

M. Li[1*], M. Lei[1] and P. H. Wen[2,1*]

[1]*College of Mathematics, Taiyuan University of Technology, Taiyuan, China*

[2] *School of Engineering and Materials Science, Queen Mary, University of London, London E1 4NS, UK*

Abstract

Based on the interpolation of Lagrange series and finite block method, the formulations of the boundary node Petrov-Galerkin method (BNPGM) are presented in weak form in this paper and the applications are demonstrated to the elasticity of functionally graded materials subjected to static and dynamic loads. By introducing the mapping technique, a block of quadratic type is transformed from the Cartesian coordinate to the normalized coordinate with 8 seeds for two dimensional problems. The first order partial differential matrices of boundary nodes are obtained in terms of the nodal values of boundary node, which can be utilized to determine the tractions on the boundary. Time dependent partial differential equations are analyzed in the Laplace transformed domain and the Durbin's inversion method is applied to determine physical values in the time domain. Illustrative numerical examples are given and comparison has been made with analytical solutions, boundary element method and finite element method.

Key words: Meshless local Petrov-Galerkin method, partial differential matrix, mapping, Lagrange interpolation, functionally graded media, Laplace transform.

*Corresponding author: Email liming01@tyut.edu.cn or p.h.wen@qmul.ac.uk

1. Introduction

Due to the complexity of the irregular boundary configurations and the material properties in general engineering problems, it is very difficult to obtain the analytical solutions. Very few analytical solutions are available in the literature books and publications which can be used as benchmarks. There are many numerical techniques available for solving differential equations. These include the Finite Difference Method (FDM), Finite Element Method (FEM), Boundary Element Method (BEM) [1]. In spite of the great success of the FEM and BEM as effective numerical tools for the solution of boundary value problems in piezoelectric solids, there is still a growing interest in the development of new advanced numerical methods. In recent years, meshless formulations are becoming popular due to their high adaptively and low cost to prepare input and output data for numerical analysis. These meshless approaches provide a new way to deal with complicated problems in engineering [2,3]. The meshless algorithms include MFS (Method of Fundamental Solution) [4,5,6,7], SPH (Smooth Particle Hydrodynamics Method) [8,9,10], DEM (Diffuse Element Method) [11], EFG (Element Free Galerkin Method) [12,13,14] and MLPG (Meshless Local Petrov-Galerkin Method) [15-19] etc. In methods based on local weak-form no background cells are required and therefore they yield the possibility to develop truly meshless methods. The meshless local Petrov-Galerkin (MLPG) method is a fundamental base for the derivation of many meshless formulations, since trial and test functions can be chosen from different functional spaces [20,21].

The main advantage of the boundary element method is that the mesh can be applied on the boundary only so that the dimension of the problem is reduced by introducing the fundamental solutions. For linear elasticity with isotropic and homogenous materials, we have the displacements on the boundary in terms of the boundary integrals without body forces as [1]

$$C_{ij}(\mathbf{x})u_j(\mathbf{x}) = \int_\Gamma U_{ij}(\mathbf{x},\mathbf{x}')t_j(\mathbf{x}')d\Gamma(\mathbf{x}') - \int_\Gamma T_{ij}(\mathbf{x},\mathbf{x}')u_j(\mathbf{x}')d\Gamma(\mathbf{x}') \tag{1}$$

where $U_{ij}(\mathbf{x},\mathbf{x}')$ and $T_{ij}(\mathbf{x},\mathbf{x}')$ are fundamental solutions, $u_i(\mathbf{x}')$ is the displacement, $\mathbf{x}$ and $\mathbf{x}'$ are source and field points, $t_i(\mathbf{x}')$ and $u_i(\mathbf{x}')$ are traction and displacement on the boundary, C_{ij} is boundary parameter. The linear system equations can be obtained by introducing boundary element with shape functions in the matrix form as

$$\mathbf{Hu} = \mathbf{Gt} \tag{2}$$

However, the fundamental solutions for general problems such as non homogenous material and functionally graded materials are not valid. Even for non-zero body forces, there are two or three domain integrals to be determined and therefore the characteristic of boundary element is disappeared. The boundary node Petrov-Galerkin method is formulated based on Lagrange interpolation and the Finite Block Method (FBM) which was proposed to solve the heat conduction problem in the functionally graded media and anisotropic materials by Wen et al [22] and Li and Wen [23] with high degree of accuracy. The physical domain is divided into several blocks (like elements in the FEM) and the continuities of the displacement and traction on the interfaces are satisfied. It has been proved that all components of stress are continuous along the interface. With the quadratic type of element (block) being transformed from physical domain to normalized domain with 8 seeds, any order of partial differential matrices is calculated by the first order differential matrices in the transformed normalized domain with the uniformly distributed collocation points. By introducing test function for all collocation points in the domain, all nodal displacements can be written in a matrix form in terms of the displacements on the boundary. Thereafter the first partial differential matrices can be obtained in terms of boundary values of displacement too. Finally one can obtain traction equations with boundary displacements similar to that of BEM in Eq.(2). The boundary node Petrov-Galerkin method in weak form is proposed to deal with engineering problems of functionally graded materials in this paper. It is apparent that the boundary node Petrov-Galerkin method is of the characteristics of the boundary element method. However, BEPGM does not need fundamental solutions to establish the relationship between the traction and displacement on the boundary. To demonstrate the accuracy and efficiency of the BNPGM, several numerical examples are given for two dimensional problems.

2. Lagrange interpolation for two-dimensions

Consider a set of two-dimensional uniformly distributed nodes shown in Figure 1, $\xi_i = -1 + 2(i-1)/(M-1)$ $(i = 1,2,...,M)$, $\eta_j = -1 + 2(j-1)/(N-1)$ $(j = 1,2,...,N)$, (ξ_i, η_j) are defined as location of node $(\bar{ij})$ and $\bar{ij} = (j-1)M + i$. Smooth function $u(\xi, \eta)$ is approximated, by using Lagrange series interpolation, as

$$u(\xi,\eta)=\sum_{i=1}^{M}\sum_{j=1}^{N}\prod_{\substack{m=1\\m\neq i}}^{M}\frac{(\xi-\xi_m)}{(\xi_i-\xi_m)}\prod_{\substack{n=1\\n\neq j}}^{N}\frac{(\eta-\eta_n)}{(\eta_j-\eta_n)}u^{\bar{i}\bar{j}}=\sum_{i=1}^{M}\sum_{j=1}^{N}F(\xi,\xi_i)G(\eta,\eta_j)u^{\bar{i}\bar{j}}. \tag{3}$$

The number of total nodes $L=M\times N$. Then, the first order partial differential is determined easily with respects to ξ is

$$\frac{\partial u}{\partial \xi}=\sum_{i=1}^{M}\sum_{j=1}^{N}\frac{\partial F(\xi,\xi_i)}{\partial \xi}G(\eta,\eta_j)u^{\bar{i}\bar{j}}, \tag{4}$$

and the first order partial differential with respects to η

$$\frac{\partial u}{\partial \eta}=\sum_{i=1}^{M}\sum_{j=1}^{N}F(\xi,\xi_i)\frac{\partial G(\eta,\eta_j)}{\partial \eta}u^{\bar{i}\bar{j}}, \tag{6}$$

where

$$\frac{\partial F(\xi,\xi_i)}{\partial \xi}=\frac{\partial}{\partial \xi}\prod_{\substack{m=1,\\m\neq i}}^{M}\frac{(\xi-\xi_m)}{(\xi_i-\xi_m)}=\sum_{l=1}^{M}\prod_{k=1,k\neq i,k\neq l}^{M}(\xi-\xi_k)/\prod_{m=1,m\neq i}^{M}(\xi_i-\xi_m), \tag{5}$$

$$\frac{\partial G(\eta,\eta_j)}{\partial \eta}=\frac{\partial}{\partial \eta}\prod_{\substack{n=1,\\n\neq j}}^{N}\frac{(\eta-\eta_n)}{(\eta_j-\eta_n)}=\sum_{l=1}^{N}\prod_{k=1,k\neq i,k\neq l}^{N}(\eta-\eta_k)/\prod_{n=1,n\neq j}^{N}(\eta_j-\eta_n). \tag{7}$$

For two-dimensional problems, one block with four sides can be mapped into a normalized domain Ω' by using the quadratic shape functions with 8 seeds. The coordinate transform (mapping) can be fulfilled with

$$x=\sum_{l=1}^{8}N_l(\xi,\eta)x_l,\ \ y=\sum_{l=1}^{8}N_l(\xi,\eta)y_l, \tag{8}$$

where (x_l, y_l) is the coordinate of seed l in real domain. The shape functions of quadratic element are given by

$$N_l(\xi,\eta)=\frac{1}{4}(1+\xi_l\xi)(1+\eta_l\eta)(\xi_l\xi+\eta_l\eta-1)\quad \text{for}\quad l=1,2,3,4 \tag{9a}$$

$$N_l(\xi,\eta)=\frac{1}{2}(1-\xi^2)(1+\eta_l\eta)\qquad \text{for}\quad l=5,7, \tag{9b}$$

$$N_l(\xi,\eta)=\frac{1}{2}(1-\eta^2)(1+\xi_l\xi)\qquad \text{for}\quad l=6,8. \tag{9c}$$

For partial differentials of function $u(x,y)$, one has

$$\frac{\partial u}{\partial x}=\frac{1}{J}\left(\beta_{11}\frac{\partial u}{\partial \xi}+\beta_{12}\frac{\partial u}{\partial \eta}\right),\ \ \frac{\partial u}{\partial y}=\frac{1}{J}\left(\beta_{21}\frac{\partial u}{\partial \xi}+\beta_{22}\frac{\partial u}{\partial \eta}\right), \tag{10}$$

where

$$\beta_{11}=\frac{\partial y}{\partial \eta},\beta_{12}=-\frac{\partial y}{\partial \xi},\beta_{21}=-\frac{\partial x}{\partial \eta},\beta_{22}=\frac{\partial x}{\partial \xi},\ J=\beta_{22}\beta_{11}-\beta_{21}\beta_{12}, \tag{11}$$

in which $\beta_{\alpha\gamma}$ $(\alpha,\gamma=1,2)$ can be obtained from Eq.(11). Therefore, the first order partial differentials can be obtained, in terms of nodal values of u, as

$$\begin{aligned}\frac{\partial u}{\partial x}&=\frac{1}{J}\sum_{i=1}^{M}\sum_{j=1}^{N}\left[\beta_{11}\frac{\partial F(\xi,\xi_i)}{\partial \xi}G(\eta,\eta_j)+\beta_{12}F(\xi,\xi_i)\frac{\partial G(\eta,\eta_j)}{\partial \eta}\right]u^{\bar{ij}},\\ \frac{\partial u}{\partial y}&=\frac{1}{J}\sum_{i=1}^{M}\sum_{j=1}^{N}\left[\beta_{21}\frac{\partial F(\xi,\xi_i)}{\partial \xi}G(\eta,\eta_j)+\beta_{22}F(\xi,\xi_i)\frac{\partial G(\eta,\eta_j)}{\partial \eta}\right]u^{\bar{ij}}.\end{aligned} \tag{12}$$

In addition, the nodal values of the first order partial differentials Eq.(12) can be written in matrix form as

$$\mathbf{u}_{,x}=\mathbf{D}_x\mathbf{u}\ ,\ \mathbf{u}_{,y}=\mathbf{D}_y\mathbf{u}, \tag{13}$$

where

$$\mathbf{u}_{,x}=\left\{\frac{\partial u(\mathbf{x}_1)}{\partial x},\frac{\partial u(\mathbf{x}_2)}{\partial x},...,\frac{\partial u(\mathbf{x}_L)}{\partial x}\right\}^{\mathrm{T}},\mathbf{u}_{,y}=\left\{\frac{\partial u(\mathbf{x}_1)}{\partial y},\frac{\partial u(\mathbf{x}_2)}{\partial y},...,\frac{\partial u(\mathbf{x}_L)}{\partial y}\right\}^{\mathrm{T}}. \tag{14}$$

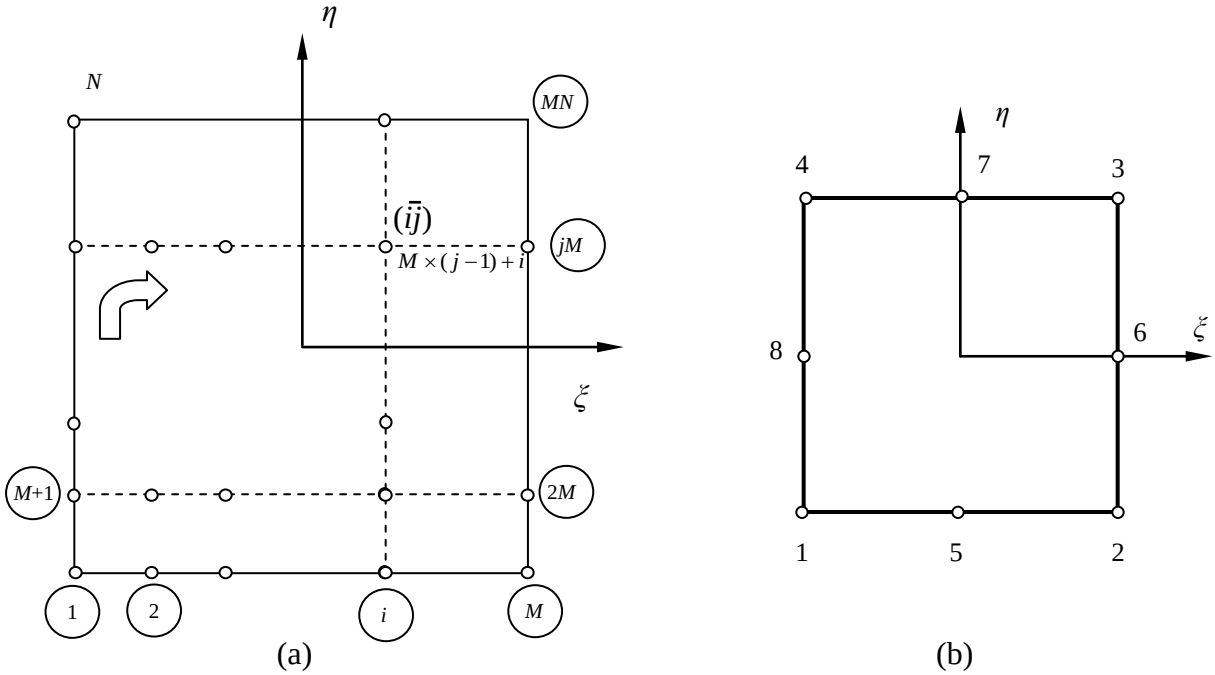

Figure 1. Two-dimensional node distribution in normalised domain: (a) the uniform distribution of nodes; (b) the quadratic element with 8 seeds.

3. Static boundary node Petrov-Galerkin method

Consider 2D elasticity plate of domain Ω with boundary Γ with functionally graded media. It is assumed that the material properties are dependent on the spatial coordinates. The equilibrium equations are

$$\begin{aligned} &\frac{\partial \sigma_x}{\partial x}+\frac{\partial \tau_{xy}}{\partial y}+b_x=0 \\ &\frac{\partial \tau_{xy}}{\partial x}+\frac{\partial \sigma_y}{\partial y}+b_y=0 \end{aligned} \qquad \mathbf{X}\in\Omega \tag{15}$$

where b_x and b_y are body forces and the relationship between stress and strain for continuously homogeneous composites are

$$\sigma_x=Q_{11}\frac{\partial u}{\partial x}+Q_{12}\frac{\partial v}{\partial y},\sigma_y=Q_{12}\frac{\partial u}{\partial x}+Q_{22}\frac{\partial v}{\partial y},\tau_{xy}=Q_{66}\left(\frac{\partial u}{\partial y}+\frac{\partial v}{\partial x}\right), \tag{16}$$

where *u* and *v* denote the displacements,

$$Q_{11}=\frac{E_1}{1-\nu_{12}\nu_{21}},\ Q_{12}=\frac{\nu_{12}E_1}{1-\nu_{12}\nu_{21}},\ Q_{22}=\frac{E_2}{1-\nu_{12}\nu_{21}},\ Q_{66}=G \tag{17}$$

where $E_1,E_2,\nu_{12},\nu_{21}$ and G are the material coefficients, which are functions of coordinate *x* and *y* for functionally graded materials. The boundary conditions can be given as

$$\begin{aligned} &u=\bar{u}(\mathbf{x}_i),\quad v=\bar{v}(\mathbf{x}_i), && \mathbf{x}_i\in\Gamma_u \\ &\sigma_x n_x+\tau_{xy}n_y=\bar{t}_x(\mathbf{x}_i),\quad \tau_{xy}n_x+\sigma_y n_y=\bar{t}_y(\mathbf{x}_i), && \mathbf{x}_i\in\Gamma_t \end{aligned} \tag{18}$$

where all variables with bar are specified boundary values, $\mathbf{n}(n_x,n_y)$ is the normal outward to the boundary. Several algorithms can be categorized as

3.1. System equations in strong form (FBM)

By using the first order differential matrices $\mathbf{D}_x$ and $\mathbf{D}_y$ in Eq.(12), the equilibrium equations become

$$\begin{aligned} &\mathbf{D}_x\left(\mathbf{Q}_{11}\mathbf{D}_x\mathbf{u}_x+\mathbf{Q}_{12}\mathbf{D}_y\mathbf{u}_y\right)+\mathbf{D}_y\mathbf{Q}_{66}\left(\mathbf{D}_y\mathbf{u}_x+\mathbf{D}_x\mathbf{u}_y\right)+\mathbf{b}_x=\mathbf{0} \\ &\mathbf{D}_x\mathbf{Q}_{66}\left(\mathbf{D}_y\mathbf{u}_x+\mathbf{D}_x\mathbf{u}_y\right)+\mathbf{D}_y\left(\mathbf{Q}_{11}\mathbf{D}_x\mathbf{u}_x+\mathbf{Q}_{12}\mathbf{D}_y\mathbf{u}_y\right)+\mathbf{b}_y=\mathbf{0} \end{aligned} \qquad \mathbf{X}\in\Omega_k,k=1,2,...,L_{\text{in}} \tag{19}$$

where $\mathbf{u}_x=\{u_i\}^T$, $\mathbf{u}_y=\{v_i\}^T$, $\mathbf{Q}_{ij}=\text{diag}\left[Q_{ij}(\mathbf{X}_k)\right]$ and L_{in} is the number of collocation points in the domain Ω. Eq.(17) can be written in matrix form as

$$\mathbf{A}_0\mathbf{u}=-\mathbf{b} \tag{20}$$

where $\mathbf{u}=[u^1,v^1,u^2,v^2,...,u^L,v^L]^{\mathrm{T}}$, $\mathbf{b}=\{b_x^1,b_y^1,...,b_x^{L_{\mathrm{in}}},b_y^{L_{\mathrm{in}}}\}^{\mathrm{T}}$ are the nodal value vectors of the displacement and forces.

3.2. Localised Petrov-Galerkin approach (PGFBM1)

In the local Petrov-Galerkin approaches, the weak form of the governing equation over a local domain Ω_k centred at point $\mathbf{x}_k$ can be written as

$$\int_{\Omega_k}\left(\frac{\partial\sigma_x}{\partial x}+\frac{\partial\tau_{xy}}{\partial y}+b_x\right)u^*d\Omega=0,\quad \int_{\Omega_k}\left(\frac{\partial\tau_{xy}}{\partial x}+\frac{\partial\sigma_y}{\partial y}+b_y\right)u^*d\Omega=0,\ \Omega_k\in\Omega,k=1,2,...,L_{\mathrm{in}} \quad (21)$$

where u^* is a test function. By the divergence theorem, Eq.(21) can be rewritten in a weak form as

$$\begin{aligned}&\int_{\Gamma_k}\left(\sigma_x n_x+\tau_{xy}n_y\right)u^*d\Gamma-\int_{\Omega_k}\left(\sigma_x\frac{\partial u^*}{\partial x}+\tau_{xy}\frac{\partial u^*}{\partial y}-b_x u^*\right)d\Omega=0,\\&\int_{\Gamma_k}\left(\tau_{xy}n_x+\sigma_y n_y\right)u^*d\Gamma-\int_{\Omega_k}\left(\tau_{xy}\frac{\partial u^*}{\partial x}+\sigma_y\frac{\partial u^*}{\partial y}-b_y u^*\right)d\Omega=0,\end{aligned}\qquad \mathbf{X}\in\Omega_k \quad (22)$$

where Γ_k is the boundary of the local integral domain Ω_k. The simplest choice of the test function is a unit step function in each local domain (PGFBM1), as follows

$$u^*(\mathbf{x})=\begin{cases}1 & \text{at } \mathbf{x}\in\Omega_k,\\ 0 & \text{at } \mathbf{x}\notin\Omega_k.\end{cases} \quad (23)$$

Then the governing equation in the local weak form (15) is written as

$$\begin{aligned}&\int_{\Gamma_k}\left(\sigma_x n_x+\tau_{xy}n_y\right)d\Gamma(\mathbf{x}')+\int_{\Omega_k}b_x d\Omega(\mathbf{X}')=0,\\&\int_{\Gamma_k}\left(\tau_{xy}n_x+\sigma_y n_y\right)d\Gamma(\mathbf{x}')+\int_{\Omega_k}b_y d\Omega(\mathbf{X}')=0.\end{aligned}\qquad \mathbf{X}\in\Omega_k,k=1,2,...,L_{\mathrm{in}} \quad (24)$$

From Eqs (16) and (12), one has

$$\begin{aligned}\sigma_x(\mathbf{x}')&=\frac{Q_{11}}{J}\sum_{i=1}^{M}\sum_{j=1}^{N}\left(\beta_{11}\frac{\partial F_i}{\partial\xi}G_j+\beta_{12}F_i\frac{\partial G_j}{\partial\eta}\right)u^{ij}+\frac{Q_{12}}{J}\sum_{i=1}^{M}\sum_{j=1}^{N}\left(\beta_{21}\frac{\partial F_i}{\partial\xi}G_j+\beta_{22}F_i\frac{\partial G_j}{\partial\eta}\right)v^{ij},\\\sigma_y(\mathbf{x}')&=\frac{Q_{12}}{J}\sum_{i=1}^{M}\sum_{j=1}^{N}\left(\beta_{11}\frac{\partial F_i}{\partial\xi}G_j+\beta_{12}F_i\frac{\partial G_j}{\partial\eta}\right)u^{ij}+\frac{Q_{22}}{J}\sum_{i=1}^{M}\sum_{j=1}^{N}\left(\beta_{21}\frac{\partial F_i}{\partial\xi}G_j+\beta_{22}F_i\frac{\partial G_j}{\partial\eta}\right)v^{ij},\\\tau_{xy}(\mathbf{x}')&=\frac{Q_{66}}{J}\sum_{i=1}^{M}\sum_{j=1}^{N}\left(\beta_{21}\frac{\partial F_i}{\partial\xi}G_j+\beta_{22}F_i\frac{\partial G_j}{\partial\eta}\right)u^{ij}+\frac{Q_{66}}{J}\sum_{i=1}^{M}\sum_{j=1}^{N}\left(\beta_{11}\frac{\partial F_i}{\partial\xi}G_j+\beta_{12}F_i\frac{\partial G_j}{\partial\eta}\right)v^{ij}.\end{aligned} \quad (25)$$

In order to evaluate the local boundary integrals in Eq.(24), a local integral domain is selected as a circle of radius r centred at (ξ_k, η_k) in the normalized domain $(\xi o \eta)$ which corresponds to the point $\mathbf{X}_k$ in the real Cartesian coordinate (xoy). Therefore, the coordinate of local integral boundary $S'(\xi_s, \eta_s)$ in the mapping domain shown in Figure 2 is

$$\xi_s = \xi_k + r\cos\theta,\ \eta_s = \eta_k + r\sin\theta \tag{26}$$

and in the practical domain, the coordinate $S(x_s, y_s)$

$$x_s = \sum_{l=1}^{8} N_l(\xi_s, \eta_s)x_l,\ y_s = \sum_{l=1}^{8} N_l(\xi_s, \eta_s)y_l \tag{27}$$

The components of the line segment are

$$\begin{aligned} dx &= rd\theta \sum_{l=1}^{8} \left\langle -\frac{\partial N_l(\xi,\eta)}{\partial \xi}\sin\theta + \frac{\partial N_l(\xi,\eta)}{\partial \eta}\cos\theta \right\rangle x_l = f(\xi_s, \eta_s) rd\theta \\ dy &= rd\theta \sum_{l=1}^{8} \left\langle -\frac{\partial N_l(\xi,\eta)}{\partial \xi}\sin\theta + \frac{\partial N_l(\xi,\eta)}{\partial \eta}\cos\theta \right\rangle y_l = g(\xi_s, \eta_s) rd\theta \end{aligned} \tag{28}$$

Thus the relationship between these two segments of length shown in Figure 4 is

$$ds = \sqrt{dx^2 + dy^2} = \sqrt{f^2 + g^2}\, rd\theta = \sqrt{f^2 + g^2}\, ds'. \tag{29}$$

Therefore, the tangential at point $S(x_s, y_s)$ in the practical domain is obtained by

$$\alpha = \tan^{-1}\frac{dy}{dx} = \frac{f}{g} \tag{30}$$

and the components of normal outward to the boundary in Eq.(24) are

$$n_x = \cos\beta,\ n_y = \sin\beta,\ \beta = \alpha - \pi/2. \tag{31}$$

The weak form of governing equation (19) can be written approximately as

$$\begin{aligned} &\int_0^{2\pi} r\left(\sigma_x n_x + \tau_{xy} n_y\right)\sqrt{f^2 + g^2}\, d\theta + b_x \Omega_k = 0, \\ &\int_0^{2\pi} r\left(\tau_{xy} n_x + \sigma_y n_y\right)\sqrt{f^2 + g^2}\, d\theta + b_y \Omega_k = 0. \end{aligned} \qquad \mathbf{X} \in \Omega_k, k = 1,2,...,L_{\text{in}} \tag{32}$$

Eq.(24) can be arranged in matrix form as

$$\mathbf{A}_1\mathbf{u} = -\mathbf{\Omega}\mathbf{b} \tag{33}$$

where $\mathbf{u} = [u^1, v^1, u^2, v^2, ..., u^L, v^L]^{\mathrm{T}}$, $\mathbf{\Omega} = \text{diag}[\Omega_1, \Omega_1, ..., \Omega_{L_{\text{in}}}, \Omega_{L_{\text{in}}}]$ are the nodal value vectors of the displacement and matrix of the local domain area.

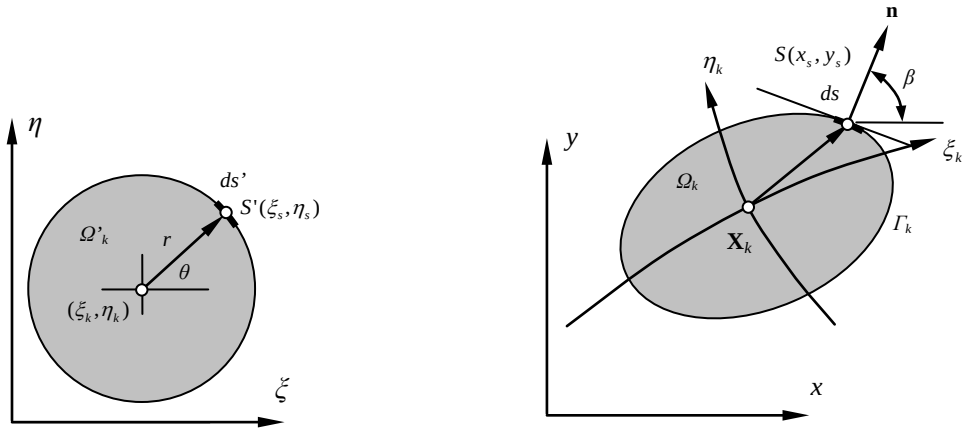

(a) (b)

Figure 2. Local integral domain and its boundary: (a) circle in normalized coordinate ($\xi o \eta$); (b) real local integral domain (xoy).

3.3. Domain Petrov-Galerkin approache (PGFBM2)

The second choice of the test function is a shape function using Lagrange series $N_k^*(\xi,\eta)$ ($\mathbf{X} \in \Omega$) in the field (PGFBM2) as

$$u^*(\mathbf{X}) = N_k^*(\xi,\eta) = F(\xi,\xi_i)G(\eta,\eta_j),\ k = M(j-1)+i,\quad \mathbf{X}_k \in \Omega \tag{34}$$

Consider the shape functions are zero on the boundary for $\mathbf{X}_k \in \Omega$, i.e.

$$\int_\Gamma \left(\sigma_x n_x + \tau_{xy} n_y\right) N_k^* d\Gamma(\mathbf{x}') = \int_\Gamma \left(\tau_{xy} n_x + \sigma_y n_y\right) N_k^* d\Gamma(\mathbf{x}') = 0 \tag{35}$$

Then the governing equation in weak form Eq.(21) is written as

$$\begin{aligned} &\int_\Omega \left(\sigma_x \frac{\partial N_k^*}{\partial x} + \tau_{xy} \frac{\partial N_k^*}{\partial y} - b_x N_k^* \right) d\Omega(\mathbf{X}') = 0, \\ &\int_\Omega \left(\tau_{xy} \frac{\partial N_k^*}{\partial x} + \sigma_y \frac{\partial N_k^*}{\partial y} - b_y N_k^* \right) d\Omega(\mathbf{X}') = 0, \end{aligned} \qquad \mathbf{X}_k \in \Omega \tag{36}$$

Substituting Eq.(25) into Eq.(29) produces a set of linear equations as

$$\mathbf{A}_2 \mathbf{u} = -\mathbf{w} \tag{37}$$

where $\mathbf{w}$ are the nodal value vectors of the domain integrals of body forces with shape functions. From Eqs (20), (33) and (37) for different algorithms, the governing equations in the field can be written as

$$\mathbf{A}\mathbf{u} = -\mathbf{w}. \tag{38}$$

If the vector of displacement is re-arranged as

$$\mathbf{u} = (\mathbf{u}_I, \mathbf{u}_B)^{\mathrm{T}},\ \mathbf{w} = (\mathbf{w}_I, \mathbf{w}_B)^{\mathrm{T}}, \tag{39}$$

where $\mathbf{u}_I (= [u^1, v^1, u^2, v^2, ..., u^{L_{\text{in}}}, v^{L_{\text{in}}}]^{\mathrm{T}})$ is the vector of displacements at internal nodes, $\mathbf{u}_B (= [u^{L_{\text{in}}+1}, v^{L_{\text{in}}+1}, ..., u^{L_{\text{in}}+P}, v^{L_{\text{in}}+P}]^{\mathrm{T}})$ is the vector of displacement on the boundary in global system, L_{in} $[= (M-2)(N-2)]$ is number of internal nodes and P $(= 2M + 2N - 4)$ is number of boundary as shown in Figure 3(b). By considering the governing Eq.(39), we have

$$(\mathbf{A}_I, \mathbf{A}_B)(\mathbf{u}_I, \mathbf{u}_B)^{\mathrm{T}} = -\mathbf{w}_I, \tag{40}$$

and solving these equations gives

$$\mathbf{u}_I = -\mathbf{A}_I^{-1}\mathbf{w}_I - \mathbf{A}_I^{-1}\mathbf{A}_B\mathbf{u}_B. \tag{41}$$

It means that the displacements $\mathbf{u}_I$, which are unknowns at internal collocation points in the domain Ω, can be represented in terms of the displacement $\mathbf{u}_B$ on the boundary. Substituting Eq.(41) into Eq.(13) results

$$\mathbf{u}_{,x} = \left(\mathbf{D}_x^B - \mathbf{D}_x^I\mathbf{A}_I^{-1}\mathbf{A}_B\right)\mathbf{u}_B - \mathbf{D}_x^I\mathbf{A}_I^{-1}\mathbf{w}_I = \mathbf{D}_x^*\mathbf{u}_B + \mathbf{D}_x^b\mathbf{b}_I, \tag{42a}$$

$$\mathbf{u}_{,y} = \left(\mathbf{D}_y^B - \mathbf{D}_y^I\mathbf{A}_I^{-1}\mathbf{A}_B\right)\mathbf{u}_B - \mathbf{D}_y^I\mathbf{A}_I^{-1}\mathbf{w}_I = \mathbf{D}_y^*\mathbf{u}_B + \mathbf{D}_y^b\mathbf{b}_I. \tag{42b}$$

Obviously the first order partial differential at each node both on the boundary and in the domain can be obtained by boundary nodal values of displacements. It is worth to notice that even for zero boundary displacements, the partial differentials with respect to both *x* and *y* are not zero due to body forces. So far, all unknowns of the system are boundary displacements $\mathbf{u}_B$ only with number *P* in total, which can be determined by considering traction boundary conditions.

As we have derived the first partial differentials in terms of the boundary nodal values of displacement in Eq.(42), the stresses are obtained sequentially

$$\sigma_x^*(\mathbf{x}_i) = Q_{11}u_{,x}^i + Q_{12}v_{,y}^i = Q_{11}\left(\sum_{j=1}^{P} D_{xij}^* u_B^j + \sum_{j=1}^{L_{\text{in}}} D_{xij}^b b_I^j\right) + Q_{12}\left(\sum_{j=1}^{P} D_{yij}^* v_B^j + \sum_{j=1}^{L_{\text{in}}} D_{yij}^b b_I^j\right),$$

$$\sigma_y^*(\mathbf{x}_i) = Q_{21}u_{,x}^i + Q_{22}v_{,y}^i = Q_{21}\left(\sum_{j=1}^{P} D_{xij}^* u_B^j + \sum_{j=1}^{L_{\text{in}}} D_{xij}^b b_I^j\right) + Q_{22}\left(\sum_{j=1}^{P} D_{yij}^* v_B^j + \sum_{j=1}^{L_{\text{in}}} D_{yij}^b b_I^j\right), \tag{43}$$

$$\tau^*_{xy}(\mathbf{x}_i) = Q_{66}u^i_{,y} + Q_{66}v^i_{,y} = Q_{66}\left(\sum_{j=1}^{P} D^*_{yij}u^j_B + \sum_{j=1}^{L_{in}} D^b_{yij}b^j_I\right) + Q_{66}\left(\sum_{j=1}^{P} D^*_{xij}v^j_B + \sum_{j=1}^{L_{in}} D^b_{xij}b^j_I\right),$$

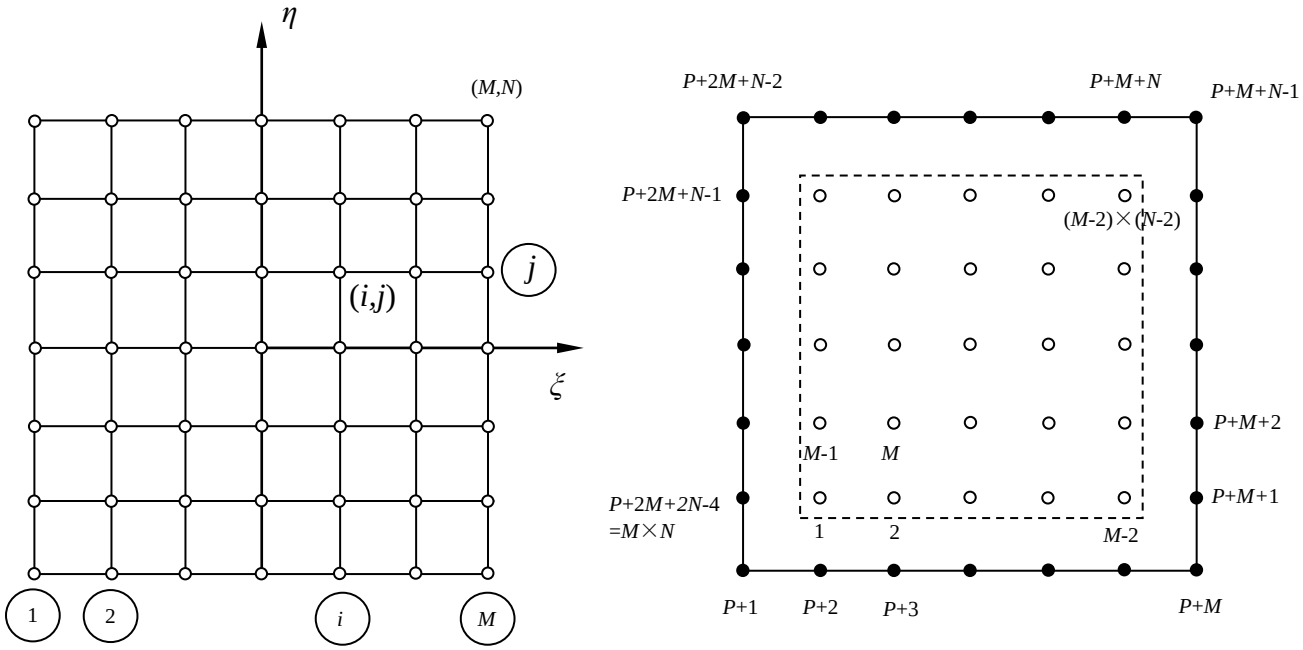

(a) (b)

Figure 3. Numbering system in normalised domain: (a) Global numbering system; (b) collocation points in the domain and on the boundary.

for $i = 1,2,...,P$ and written in matrix form

$$\begin{aligned}
\boldsymbol{\sigma}^*_x &= \boldsymbol{\alpha}_x\mathbf{b}_I + \boldsymbol{\beta}_x\mathbf{u}_B,\\
\boldsymbol{\sigma}^*_y &= \boldsymbol{\alpha}_y\mathbf{b}_I + \boldsymbol{\beta}_y\mathbf{u}_B,\\
\boldsymbol{\tau}^*_{xy} &= \boldsymbol{\alpha}_{xy}\mathbf{b}_I + \boldsymbol{\beta}_{xy}\mathbf{u}_B.
\end{aligned} \tag{44}$$

Therefore, the tractions can be arranged in matrix form, with zero body forces, as

$$\mathbf{t}_B = \mathbf{H}^*\mathbf{u}_B, \tag{45}$$

where $H^*_{2i-1,j} = \beta_{xij}n^i_1 + \beta_{xyij}n^i_2$, $H^*_{2i,j} = \beta_{xyij}n^i_1 + \beta_{yij}n^i_2$. There are following kinds of boundary conditions in solid structures:

(1) Displacement boundary

$$u^i = \bar{u}^i, v^i = \bar{v}^i \qquad \mathbf{x}_i \in \Gamma_u \quad (N_u). \tag{46}$$

(2) Traction boundary

$$t_{xi} = \sigma^*_{xi} n_x + \tau^*_{xyi} n_y, \quad t_{yi} = \tau^*_{xyi} n_x + \sigma^*_{yi} n_y \quad \mathbf{x}_i \in \Gamma_t \quad (N_t). \tag{47}$$

where $\sigma^*_{xi}, \sigma^*_{yi}$ and τ^*_{xyi} are given in Eq.(44), N_u and N_t are numbers of nodes located on the displacement and traction boundaries respectively.

(3) Free corners

$$\int_{\theta_1^i}^{\theta_2^i} \left(\sigma^*_{xi} \cos\theta + \tau^*_{xyi} \sin\theta\right) R d\theta + F_x^i = 0, \quad \int_{\theta_1^i}^{\theta_2^i} \left(\tau^*_{xyi} \cos\theta + \sigma^*_{yi} \sin\theta\right) R d\theta + F_y^i = 0 \tag{48}$$

where F_x^i and F_y^i are resultants of applied force acting on the boundary (two edges). Due to the stresses in the local area with unit radius (small) are constants as shown in Figure 4, Eq.(48) becomes

$$\begin{aligned} &\sigma^*_{xi}\left(\sin\theta_2^i - \sin\theta_1^i\right) - \tau^*_{xyi}\left(\cos\theta_2^i - \cos\theta_1^i\right) + F_x^i = 0, \\ &\tau^*_{xyi}\left(\sin\theta_2^i - \sin\theta_1^i\right) - \sigma^*_{yi}\left(\cos\theta_2^i - \cos\theta_1^i\right) + F_y^i = 0. \end{aligned} \tag{49}$$

(4) Simply supported

$$\sigma^*_{xi}\left(\sin\theta_2^i - \sin\theta_1^i\right) - \tau^*_{xyi}\left(\cos\theta_2^i - \cos\theta_1^i\right) + F_x^i = 0, \quad v^i = 0, \tag{50a}$$

or

$$\tau^*_{xyi}\left(\sin\theta_2^i - \sin\theta_1^i\right) - \sigma^*_{yi}\left(\cos\theta_2^i - \cos\theta_1^i\right) + F_y^i = 0, \quad u^i = 0\,. \tag{50b}$$

(5) Interface between two blocks

(a) If $\mathbf{x}^I = \mathbf{x}^{II}$

$$\begin{aligned} &u^I(\mathbf{x}^I) = u^{II}(\mathbf{x}^{II}), \quad v^I(\mathbf{x}^I) = v^{II}(\mathbf{x}^{II}), \\ &t_x^I(\mathbf{x}^I) + t_x^{II}(\mathbf{x}^{II}) = 0, \quad t_y^I(\mathbf{x}^I) + t_y^{II}(\mathbf{x}^{II}) = 0. \end{aligned} \qquad \mathbf{x}_i \in \Gamma_{\text{int}} \tag{51}$$

(b) If $\mathbf{x}^I \neq \mathbf{x}^{II}$

$$\begin{aligned} &u^I(\mathbf{x}^I) = u^{II}(\mathbf{x}^I), \quad v^I(\mathbf{x}^I) = v^{II}(\mathbf{x}^I), && \mathbf{x}^I \in \Gamma_{\text{int}}^I \\ &t_x^I(\mathbf{x}^{II}) + t_x^{II}(\mathbf{x}^{II}) = 0, \quad t_y^I(\mathbf{x}^{II}) + t_y^{II}(\mathbf{x}^{II}) = 0. && \mathbf{x}^{II} \in \Gamma_{\text{int}}^{II} \end{aligned} \tag{52}$$

This algorithm can be use to combine BNPGM with any other methods such as FE and BEM to deal with large scale problems in engineering. It does mean that for the local study such as fracture and damage analysis, we can ABAQUS subroutine function to study `more complicated practical problems.

(6) Joint with X blocks (shown in Figure 4)

$$u^I(\mathbf{x}_i) = u^{II}(\mathbf{x}_i) = ... = u^X(\mathbf{x}_i), \quad v^I(\mathbf{x}_i) = v^{II}(\mathbf{x}_i) = ... = v^X(\mathbf{x}_i), \tag{53a}$$

$$\sum_{H=I}^{X}\left[\sigma_{xi}^{*H}(\mathbf{x}_i)\left(\sin\theta_2^{iH} - \sin\theta_1^{iH}\right) - \tau_{xyi}^{*I}(\mathbf{x}_i)\left(\cos\theta_2^{iH} - \cos\theta_1^{iH}\right)\right] + F_x^i = 0, \tag{53b}$$

$$\sum_{H=1}^{X}\left[\tau_{xyi}^{*H}(\mathbf{x}_i)\left(\sin\theta_2^{iH} - \sin\theta_1^{iH}\right) - \sigma_{yi}^{*H}(\mathbf{x}_i)\left(\cos\theta_2^{iH} - \cos\theta_1^{iH}\right)\right] + F_y^i = 0. \tag{53c}$$

The last two equations are equilibriums for infinitesimal region centered at the joint $\mathbf{x}_i$.

Obviously in the case of one block, there are $2\times N_t$ linear algebraic equations only from Eq.(45) to be used to determine the displacements $\mathbf{u}_B$ on the traction boundary Γ_t. It means that for the displacement boundary condition, there are no any unknowns need to be solved, as $\mathbf{u}_B$ are given by boundary conditions $(N_t = 0)$. One of the advantages of the boundary node Petrov-Galerkin method is that the number of unknowns is reduced from $2\times L$ (two-dimension) to $2\times N_t$ (one-dimension). In general case, the equations of stresses in Eq.(45) on the boundary nodes are considered. For more than one block problem, we always have two equations for each node on the boundary either from the traction boundary condition or connect conditions on the interfaces. Recall the system equations of BEM in Eq.(2), the BNPGM possesses the same characteristics, i.e. the relationship between tractions and displacements on the boundary in Eq.(45). However, there are no requirements of the fundamental solutions in the BNPGM. Therefore, for functionally graded materials and non homogenous materials, the BNPGM can be utilized straightaway. For fully bounded interface, it is easy to prove that all stress components are continuous on the interface between two blocks, i.e. $\sigma_x^I = \sigma_x^{II}$, $\sigma_y^I = \sigma_y^{II}$ and $\tau_{xy}^I = \tau_{xy}^{II}$. Therefore, the higher accuracy of the numerical solutions are expected by using BNPGM than other methods. Compared with MLPG method, the differences are summarized as: (1) The distribution of collocation nodes is control by eight seeds of quadratic block which characteristics can be used to study stress concentrations [22]; (2) There are no free parameters in the interpolation of variables such as free parameters used in radial basis function and moving least square methods; (3) The first partial differential matrices are only needed for higher order partial differential matrices; (4) Stability is excellent for selection of

local integral domain; (5) Behaviors of the boundary element method character is maintained; (6) The stress components are continuous along the interfaces between blocks.

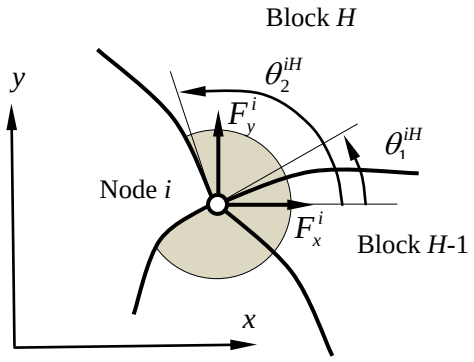

Figure 4. Joint with more than two blocks.

4. Dynamic boundary node Petrov-Galerkin method

In this chapter we consider 2D elastodynamic problems. The equilibrium equations for two dimensional problems are given as

$$\begin{aligned} &\frac{\partial \sigma_x}{\partial x}+\frac{\partial \tau_{xy}}{\partial y}+b_x=\rho\frac{\partial^2 u}{\partial t^2}, \\ &\frac{\partial \tau_{xy}}{\partial x}+\frac{\partial \sigma_y}{\partial y}+b_y=\rho\frac{\partial^2 v}{\partial t^2}, \end{aligned} \qquad \mathbf{X}\in\Omega \tag{54}$$

where ρ indicates the mass density of the plate and the boundary conditions

$$\begin{aligned} &u(\mathbf{x}_k,t)=\bar{u}(\mathbf{x}_k,t),\quad v(\mathbf{x}_k,t)=\bar{v}(\mathbf{x}_k,t), && \mathbf{x}_k\in\Gamma_u \\ &t_x(\mathbf{x}_k,t)=\bar{t}_x(\mathbf{x}_k,t),\quad t_x(\mathbf{x}_k,t)=\bar{t}_x(\mathbf{x}_k,t), && \mathbf{x}_k\in\Gamma_t \end{aligned} \tag{55}$$

for $t>0$ with following initial conditions

$$\begin{aligned} &u(\mathbf{x}_k,0)=U^0(\mathbf{x}_k),\quad \dot{u}(\mathbf{x}_k,0)=u^0(\mathbf{x}_k), \\ &v(\mathbf{x}_k,0)=V^0(\mathbf{x}_k),\quad \dot{v}(\mathbf{x}_k,0)=v^0(\mathbf{x}_k). \end{aligned} \qquad \mathbf{x}_k\in\Omega \tag{56}$$

Appling Laplace transformation over both sides of Eq.(54) gives

$$\begin{aligned}
&\frac{\partial \tilde{\sigma}_x}{\partial x}+\frac{\partial \tilde{\tau}_{xy}}{\partial y}+\tilde{b}_x=\rho\left(s^2\tilde{u}-su^0-U^0\right)\\
&\frac{\partial \tilde{\tau}_{xy}}{\partial x}+\frac{\partial \tilde{\sigma}_y}{\partial y}+\tilde{b}_y=\rho\left(s^2\tilde{v}-sv^0-V^0\right)
\end{aligned}\qquad \mathbf{X}_k\in\Omega, \tag{57}$$

where s is Laplace transform parameter and the Laplace transform of function $f(t)$ is defined as

$$\tilde{f}(s)=\int_0^\infty f(t)e^{-st}dt. \tag{58}$$

The transformed displacements and tractions satisfy the following boundary conditions:

$$\begin{aligned}
&\tilde{u}(\mathbf{x}_k,s)=\tilde{\bar{u}}(\mathbf{x}_k,s),\quad \tilde{v}(\mathbf{x}_k,s)=\tilde{\bar{v}}(\mathbf{x}_k,s) && \mathbf{x}_k\in\Gamma_u,\\
&\tilde{t}_x(\mathbf{x}_k,s)=\tilde{\bar{t}}_x(\mathbf{x}_k,s),\quad \tilde{t}_y(\mathbf{x}_k,s)=\tilde{\bar{t}}_y(\mathbf{x}_k,s) && \mathbf{x}_k\in\Gamma_t.
\end{aligned} \tag{59}$$

In the boundary node Petrov-Galerkin method (PGFBM1), the weak form of the governing equation over a local domain Ω_k centred at point $\mathbf{X}_k$ can be written as

$$\begin{aligned}
&\int_{\Omega_s}\left(\frac{\partial \tilde{\sigma}_x}{\partial x}+\frac{\partial \tilde{\tau}_{xy}}{\partial y}+\tilde{b}_x-\rho s^2\tilde{u}\right)u^*d\Omega(\mathbf{X}')=0,\\
&\int_{\Omega_s}\left(\frac{\partial \tilde{\tau}_{xy}}{\partial x}+\frac{\partial \tilde{\sigma}_y}{\partial y}+\tilde{b}_y-\rho s^2\tilde{u}\right)u^*d\Omega(\mathbf{X}')=0,
\end{aligned}\qquad \mathbf{X}_i\in\Omega \tag{60}$$

where u^* is a test function. By the divergence theorem, one has

$$\begin{aligned}
&\int_{\Gamma_s}\left(\tilde{\sigma}_x n_x+\tilde{\tau}_{xy}n_y\right)u^*d\Gamma-\int_{\Omega_s}\left(\tilde{\sigma}_x\frac{\partial u^*}{\partial x}+\tilde{\tau}_{xy}\frac{\partial u^*}{\partial y}-\tilde{b}_x u^*+\rho s^2\tilde{u}u^*\right)d\Omega(\mathbf{X}')=0,\\
&\int_{\Gamma_s}\left(\tilde{\tau}_{xy} n_x+\tilde{\sigma}_y n_y\right)u^*d\Gamma-\int_{\Omega_s}\left(\tilde{\tau}_{xy}\frac{\partial u^*}{\partial x}+\tilde{\sigma}_y\frac{\partial u^*}{\partial y}-\tilde{b}_y u^*+\rho s^2\tilde{v}v^*\right)d\Omega(\mathbf{X}')=0.
\end{aligned}\qquad \mathbf{X}_i\in\Omega \tag{61}$$

By selecting a unit step function in each local domain, one has the governing equations from Eq.(61)

$$\begin{aligned}
&\int_{\Gamma_k}\left(\tilde{\sigma}_x n_x+\tilde{\tau}_{xy}n_y\right)d\Gamma(\mathbf{x}')-\rho s^2\int_{\Omega_k}\tilde{u}d\Omega(\mathbf{X}')+\int_{\Omega_k}\tilde{b}_x d\Omega(\mathbf{X}')=0,\\
&\int_{\Gamma_k}\left(\tilde{\tau}_{xy} n_x+\tilde{\sigma}_y n_y\right)d\Gamma(\mathbf{x}')-\rho s^2\int_{\Omega_k}\tilde{v}d\Omega(\mathbf{X}')+\int_{\Omega_k}\tilde{b}_y d\Omega(\mathbf{X}')=0.
\end{aligned}\qquad \mathbf{X}_k\in\Omega_k,\ k=1,2,...,L_{\text{in}} \tag{62}$$

Following the same procedure of statics, Eq.(62) can be written approximately in matrix form as

$$\left(\mathbf{A}-\rho s^2\mathbf{\Omega}\right)\tilde{\mathbf{u}}=-\tilde{\mathbf{w}}, \tag{63}$$

where $\tilde{\mathbf{w}}=\mathbf{\Omega}\tilde{\mathbf{b}}$. If the vector of displacement is re-arranged as

$$\tilde{\mathbf{u}}=(\tilde{\mathbf{u}}_I,\tilde{\mathbf{u}}_B)^{\mathrm{T}},\ \tilde{\mathbf{w}}=(\tilde{\mathbf{w}}_I,\tilde{\mathbf{w}}_B)^{\mathrm{T}}, \tag{64}$$

Eq.(56) becomes

$$\left(\mathbf{A}_I-\rho s^2\mathbf{\Omega},\mathbf{A}_B\right)(\tilde{\mathbf{u}}_I,\tilde{\mathbf{u}}_B)^{\mathrm{T}}=-\tilde{\mathbf{w}}_I. \tag{65}$$

If the Laplace transform parameter *s* is chosen as real value, we can determine all internal displacements in terms of displacements on the boundary and body forces as

$$\tilde{\mathbf{u}}_I=-\left(\mathbf{A}_I-\rho s^2\right)^{-1}\tilde{\mathbf{w}}_I-\left(\mathbf{A}_I-\rho s^2\right)^{-1}\mathbf{A}_B\tilde{\mathbf{u}}_B. \tag{66}$$

Otherwise, we need to split each equation in complex into two equations in real, i.e. consider real part and imagine part for each equation respectively. Following the same procedure for static case, we have tractions (along the normal and tangential directions) on a smooth boundary for each block in the Laplace transform domain

$$\tilde{\mathbf{t}}_B=\tilde{\mathbf{H}}^*(s)\tilde{\mathbf{u}}_B, \tag{67}$$

where $\tilde{\mathbf{H}}^*(s)$ can be determined from Eqs (66) and (13) following the same procedure of static approach. Same again, there are only $2\times N_t$ linear algebraic equations in Eq.(67) to determine the displacements $\tilde{\mathbf{u}}_B$ on the boundary of traction Γ_t. In order to calculate time dependent values, we have to select a proper Laplace inverse technique. For the real parameter *s* in the Laplace space, Stehfest's algorithm [24] is one of the most popular methods. But the number of sample in the Laplace space is limited to 20 in the most cases. The simplest algorithm is proposed by Durbin [25] which has many advantages such as stable and accurate for large period of time. Suppose there are (*K*+1) samples in the transformation space $s_k, k=0,1,...,K$ and the same number of transformed values $\tilde{f}(s_k)$. Then, $f(t)$ can be obtained by

$$f(t)=\frac{2e^{\sigma t/T}}{T}\left[-\frac{1}{2}\tilde{f}(s_0)+\sum_{k=0}^{K}\mathrm{Re}\left\{\tilde{f}(s_k)e^{2\pi ikt/T}\right\}\right], \tag{68}$$

where the parameter of the Laplace transform is chosen as $s_k=\left(\sigma+2\pi ik\right)/T$, $(i=\sqrt{-1})$. The parameters *T* depends on the observing period in time and no dimensional parameter $\sigma=5$ [25] in general cases. In the following examples, all variables are normalized for the sake of analysis convenience.

5. Numerical examples

5.1. Square plate under shear load

A square plate of width *a* subjected to a uniformly distributed shear load τ_0 on the top with fixed bottom is considered in this example shown in Figure 5. The Poisson ratio *v*=0.3. Three algorithms (FBM, BNPGM1 and BNPGM2) are observed and compared in numerical analysis. The collocation points are uniformly distributed in the domain ($L = 11\times 11$) for BNPGM1 and BNPGM2. For these two methods, it is found that when $L(= M \times N)$ is larger than 6×6, the numerical solution is convergence rapidly. However, the maximum numbers of node for each direction are limited by $M_{\max} = N_{\max} = 21$ due to the oscillation of Lagrange series with large number of collocation point. In addition, one free parameter for BNPGM1, i.e. the size of local domain is selected as a circle of diameter *d* in the normalized domain. With different choices of the diameter in the region $0 < d < 2\Delta$, where $\Delta = 1/M$, we found that the effects of *d* on the degree of accuracy are extremely small. Therefore, the diameter of local domain is fixed to $1/M$ in all examples. To evaluate the local boundary integrals, a regular integration algorithm is adopted and the number of integration point is chosen as 18 for BNPGM1.

To illustrate the accuracy of these three methods, the solutions by the BEM [1] (64 quadratic boundary elements) are plotted for comparison in the same figures. As the fixed boundary condition on the bottom, the stresses are singular at the corners of the plate which can be seen from the results in Figures 6 and 7. It is clear that the numerical results by FBM [1] and BNPGM1 are in good agreement with the BEM results even with small number of boundary nodes ($P = 40$). For BNPGM2, in order to fulfill domain integrals, a back ground grid is introduced (400×400) and it is found that the numerical results are sensitive with the selection of the node number *M* and *N*. It is because the characteristics of oscillation for Lagrange interpolation with a bigger number of node such as $M > 7$. The results of BNPGM2 with *L*(6×6) are shown in Figures 5 and 6. In addition, it is obvious that the accuracy of BNPGM1 is higher than FBM in the same conditions.

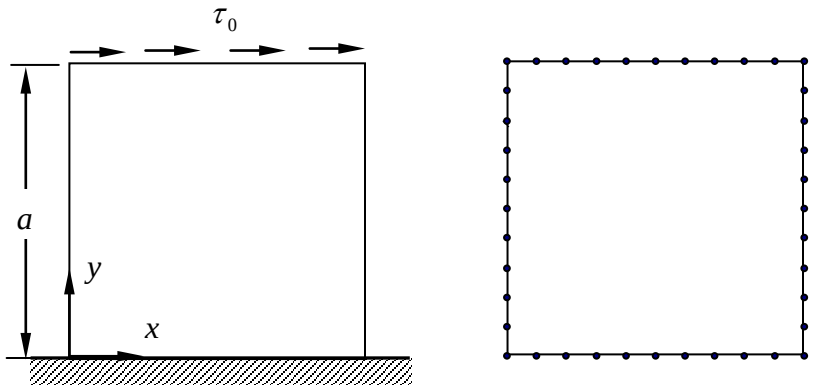

Figure 5. Square plate with one block subjected to uniform shear load on the top: (a) geometry and boundary condition; (b) boundary nodes.

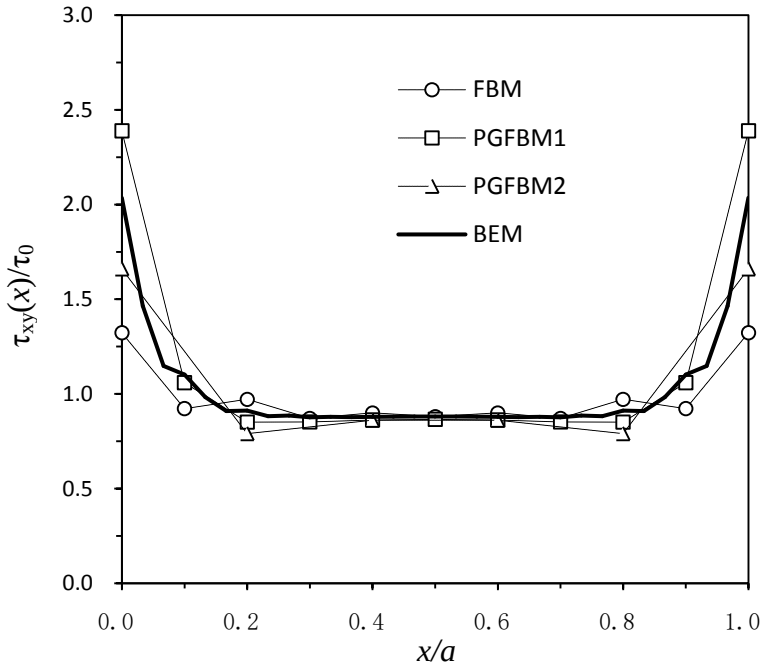

Figure 6. Distribution of normalized shear stress $\tau_{xy}(x)/\tau_0$ on the bottom.

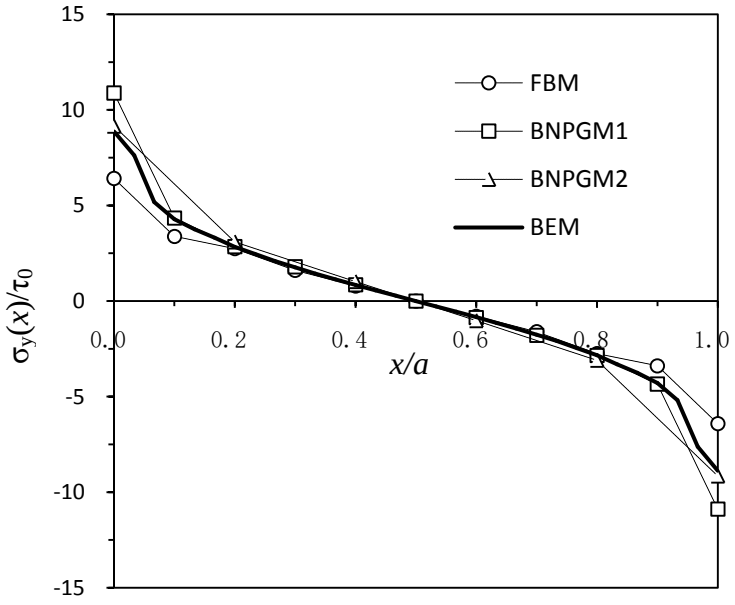

Figure 7. Distribution of normalized normal stress $\sigma_y(x)/\tau_0$ on the bottom.

5.2. Beam of functionally graded media under bending load

To demonstrate BNPGM with different numbers of collocation point on the interface between two blocks, we consider a 2D beam of length 2*L* and height *h* with functionally graded material as shown in Figure 8(a)(b) subjected to the shear load at the end. It is clamped at the left hand side. In the numerical solution, the mechanical properties of material are normalised and given: $E_1 = E_2 = E_0 e^{y \ln \lambda / h}$, $\lambda = E_h / E_0$, E_0 and E_h are Young's modulus on the bottom and top surfaces of the beam. In this case, the analytical solution by using beam theory can be obtained. With plane assumption of classical beam theory, the normal strain and normal stress on the cross-section are assumed as

$$\varepsilon_x^{\text{beam}} = \alpha(x)(y - y_0),\ \sigma_x^{\text{beam}} = E_1 \varepsilon_x^{\text{beam}} = \alpha(x) E_0 (y - y_0) e^{y \ln \lambda / h} \tag{69}$$

where y_0 is the location of neutral axis and α is function of horizontal axis *x*. Considering the equilibrium conditions of the cross section leads to

$$\int_0^h \sigma_x^{\text{beam}} dy = 0, \ \int_0^h \sigma_x^{\text{beam}} y dy = -M(x) \tag{70}$$

where $M(x)$ is bending moment at cross section x. Therefore we have

$$y_0 = h\left(\frac{\lambda}{\lambda-1} - \frac{1}{\ln\lambda}\right), \ \alpha = -\frac{M(x)(\ln\lambda)^3}{E_0 h^3 C} \tag{71}$$

where

$$C = \lambda\left((\ln\lambda)^2 - 2\ln\lambda + 2\right) - \frac{y_0}{h}\lambda(\ln\lambda - 1)\ln\lambda - 2 - \frac{y_0}{h}\ln\lambda \tag{72}$$

and the shear stress can be deduced as

$$\tau_{xy}^{\text{beam}} = \frac{\alpha E_0 h^2 S(x)}{(\ln\lambda)^2}\left[\lambda(\ln\lambda - 1) - e^{y\ln\lambda/h}(y\ln\lambda/h - 1) - a\ln\lambda/h\left(\lambda - e^{y\ln\lambda/h}\right)\right] \tag{73}$$

Consider the shear stress at the end, we have $M(x) = -\tau_0 h(2L - x)$ and $S(x) = \tau_0 h$. Then the deflection of the beam is derived, for cantilever beam shown in Figure 8(a), as

$$v^{\text{beam}}(x) = \frac{(\ln\lambda)^3 \tau_0}{6_0 h^2 C}(3L - x)x^2. \tag{74}$$

In the numerical simulation by using BNPGM, the ratio of length and height is specified as $L/h = 4$ and 2D dimension $(L \times 0.25L)$ for each block. There are $L^I (= M^I \times N^I)$ and $L^{II} (= M^{II} \times N^{II})$ nodes uniformly distributed in each block shown in Figure 5(b), here $M^{II} = M^I - 1$ and $N^{II} = N^I - 1$ in this example for simplicity. Poisson ratios are assumed $\nu_{12} = \nu_{21} = 0$, $G = E_1/2(1+\nu_{12})$ in Eq.(16) and $\lambda = 10$. To observe the convergence of the algorithms, different densities of nodes are considered, i.e. $L^I (= 16 \times 8$ and $19 \times 11)$. Figures 9 and 10 show the variations of the normal stress $\sigma_x(y)$ and shear stress $\tau_{xy}(y)$ on the interface between two blocks at $x = L$. The normalized deflection $v(x)$ on the top surface $y = h$ is shown in Figure 11. The analytical solutions of the classical beam are shown in these figures for comparison. The convergence by BNPGM is clear for all numerical solutions and the agreements between them are excellent.

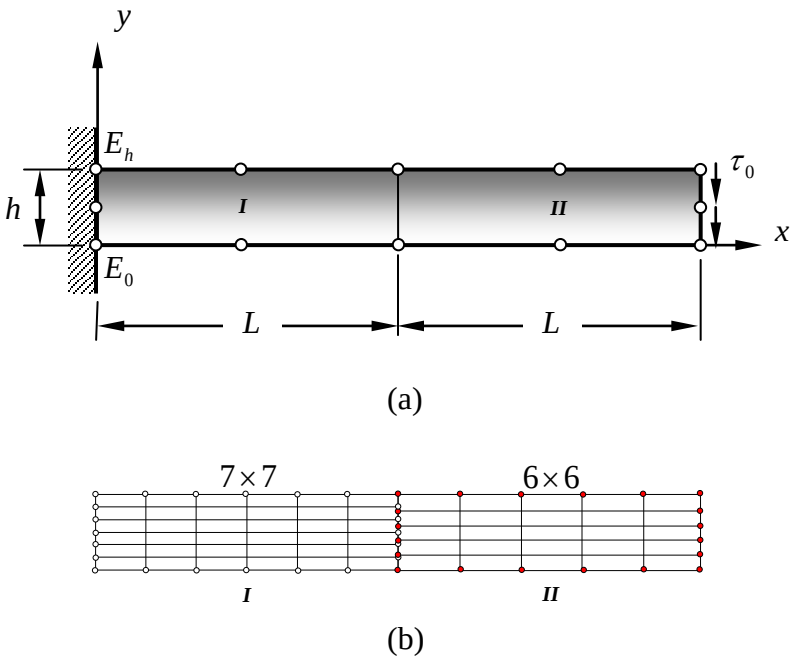

Figure 8. Cantilever beam with two blocks: (a) mapping seeds; (b) uniformly distributed boundary nodes with different node densities for each block.

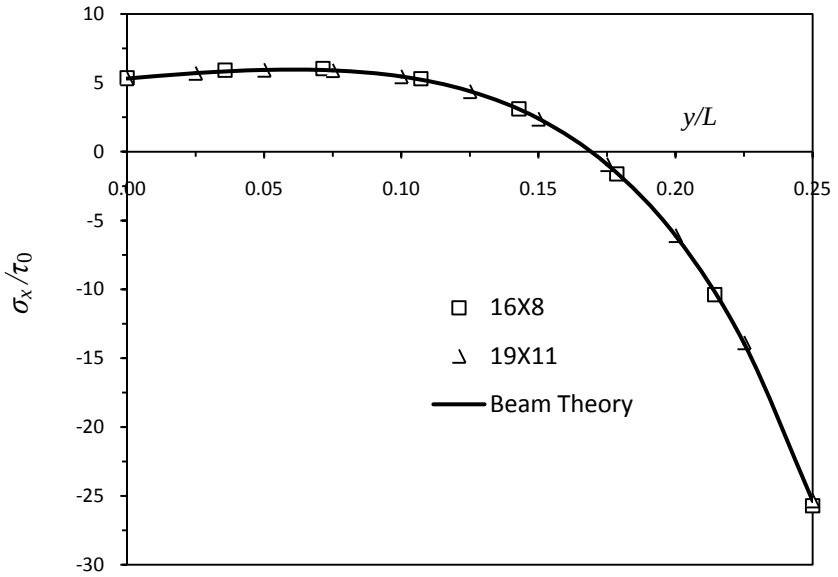

Figure 9. Normal stress distribution at middle section of beam σ_x / τ_0 when $x = L$.

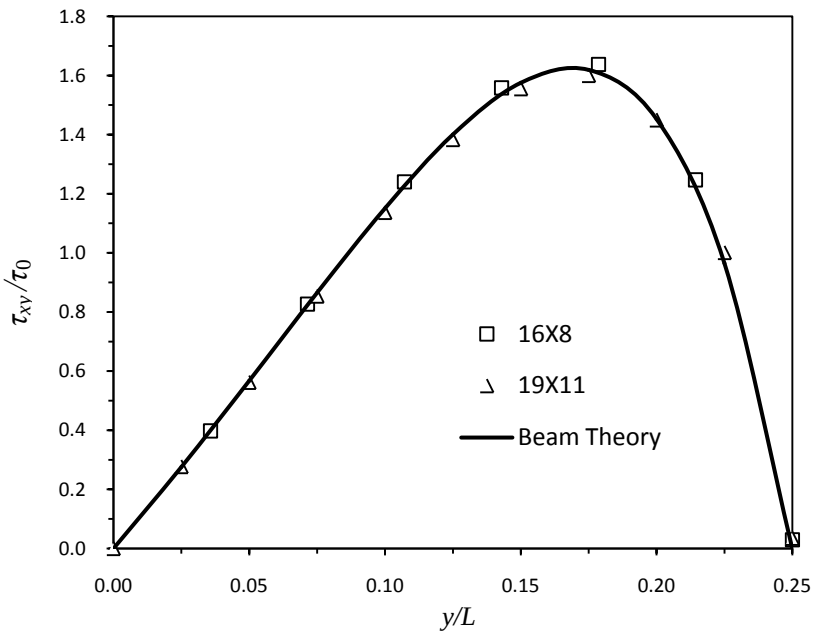

Figure 10 Shear stress distribution at middle section of beam τ_{xy}/τ_0 when $x = L$.

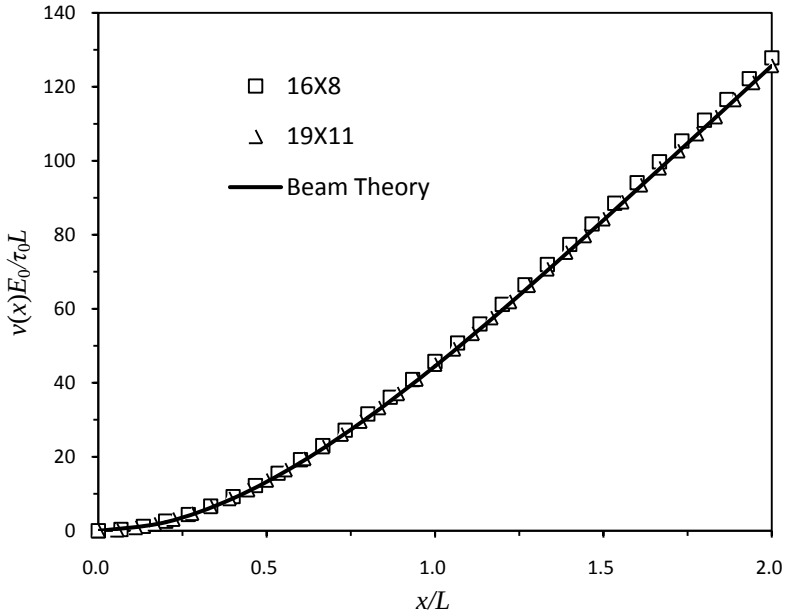

Figure 11. Deflection of cantilever beam of top surface $-v(x)E_0/(\tau_0 L)$ when $y = h$.

5.3. Square plate with a hole under tension

A square plate of width *a* containing a square hole of width *a*/2 is subjected to a uniform tension σ_0 both on top and bottom of the plate. Due to the symmetry of geometry and the loading condition, only a quarter of the plate is analysed shown in Figure 12. Poisson's ratio v=0.3. Three blocks are used in this case and the node density is chosen as 11×11 for each block. Then there are 363 nodes in total, two interfaces and two joints. Normalized stress distributions of σ_y / σ_0 on the bottom $y = 0$ and on the interface $y = a/2$ are plotted in the Figure 13. In addition, Figure 14 shows the normalized displacements $uE/\sigma_0 a$ and $vE/\sigma_0 a$ on the top of the plate. The results given by BEM (128 quadratic elements) and meshless method [26] with radial basis functions interpolation (RBF) (768 nodes) are plotted in the same figure for comparison. Good agreement with the BEM results has been achieved both for the stress and displacement. The accuracy of BNPGM is found to be much higher with less nodes than meshless method (RBF) seeing from the stress concentration at the corner of the inner hole.

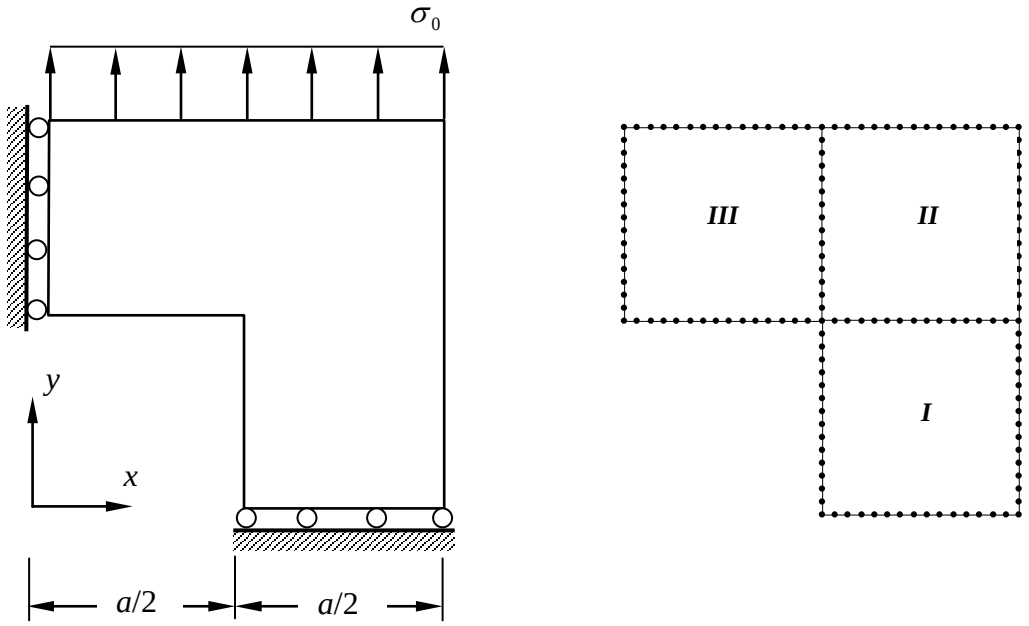

Figure12. A square plate with a hole: (a) geometry and working condition; (b) blocks with boundary nodes.

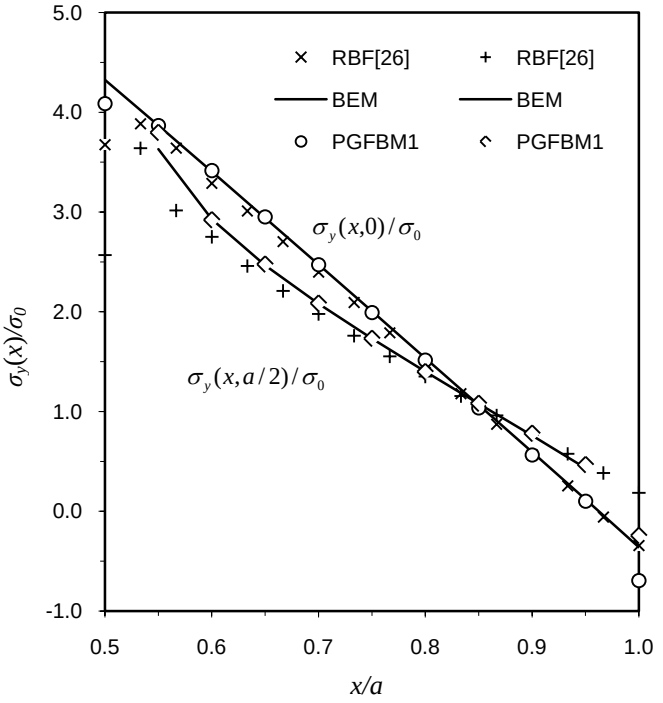

Figure 13. Normalized stresses on different sections.

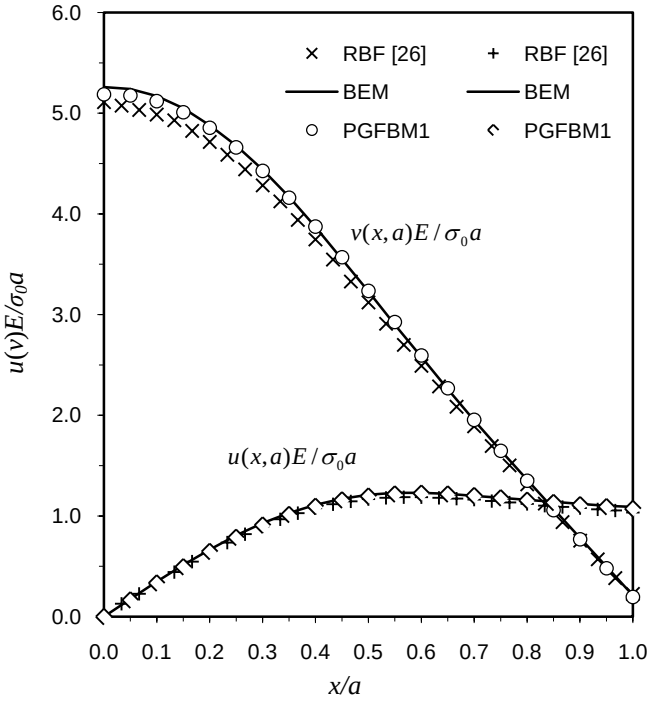

Figure 14. Normalized displacements on the top of the plate.

5.4. Square plate containing a circular hole under static and dynamic loads

Consider a quarter of a square plate of width *a* containing a circular hole of radius *R* subjected to the uniformly distributed load σ_0 on the top as shown in Figure 15. In order to consider the degree of accuracy with finite element method, the isotropic material is assumed with assumptions $R = a/2$, Young's modulus $E_1 = E_2 = E$ and Poisson ratio $\nu = 0.3$. Two blocks are employed with node density 11×11 and the distribution of collocation point with 13 mapping seeds is shown in Figure 15(b). On the interface between these two blocks ($\eta^I = +1$ and $\eta^{II} = -1$), both continuous conditions for displacement and traction on the interface have to be satisfied for each node, i.e. $u^I = u^{II}$, $v^I = v^{II}$, $t_x^I + t_x^{II} = 0$ and $t_y^I + t_y^{II} = 0$. To compare with other numerical method, the solutions given by FEM(ABAQUS) with 30047 nodes are compared. Figures 16 and 17 show the stresses σ_y and σ_x respectively from A to B and from C to D respectively. The stress concentration can be seen clearly along the circular hole. Apparently, excellent agreements between these two methods have been achieved under static load.

Finally we consider dynamic case with a uniformly load $\sigma_0 H(t)$ acting on the top, where $H(t)$ is Heaviside function. Free parameter *T* in Durbin inversion formula Eq.(68) is chosen as $60t_0$, where $t_0 = a/c$, $c = \sqrt{E/\rho}$. Same working conditions including material properties, geometry and node distribution in the static case are kept here. The normalized time dependent stresses, $\sigma_y(t)/\sigma_0$ at point A and B and $\sigma_x(t)/\sigma_0$ at point C and D, versus the normalised time ct/a are plotted in Figures 18 and 19 respectively. We can see that all stresses in Figure 18 should maintain to zero before the longitudinal elastic wave arrival travelling from the top of the plate to points A and B, i.e. $t^* = a/c_1$, here $c_1 = \left(E(1-\nu)/(1+\nu)(1-2\nu)\rho\right)^{1/2}$. In addition, the horizontal dash lines in the figures indicate the values of stress under static load. Obviously the dynamic stresses oscillate about their levels of static value respectively for each location. One can observe a good accuracy in the whole time interval under dynamic load with the Laplace transform technique and Durbin inversion algorithm.

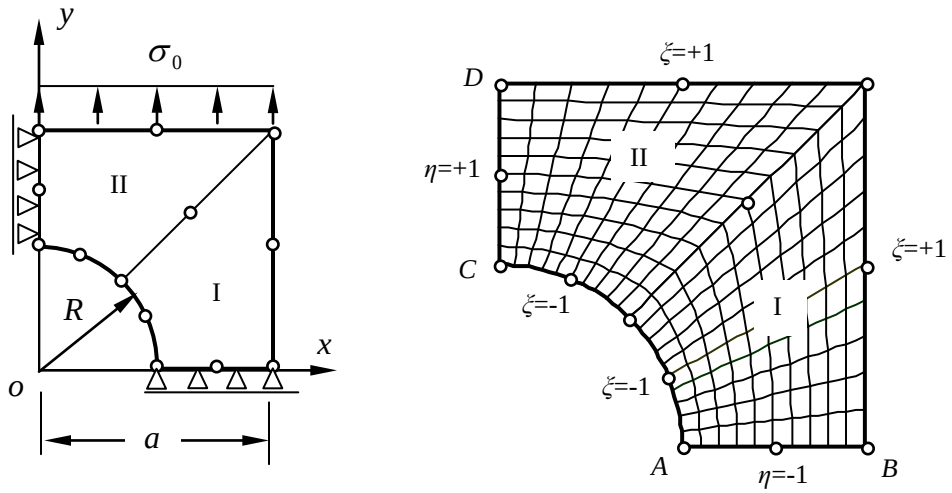

(a) (b)

Figure 15. Blocks of a quarter square plate and their mapping seeds: (a) geometry and constrain conditions; (b) distributions of node for two blocks.

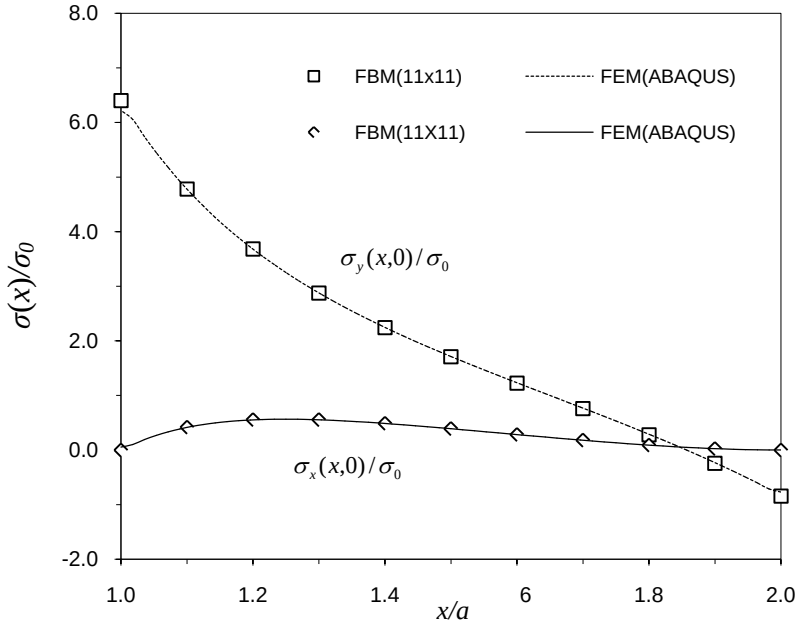

Figure 16. Normalized stresses along axis *x*.

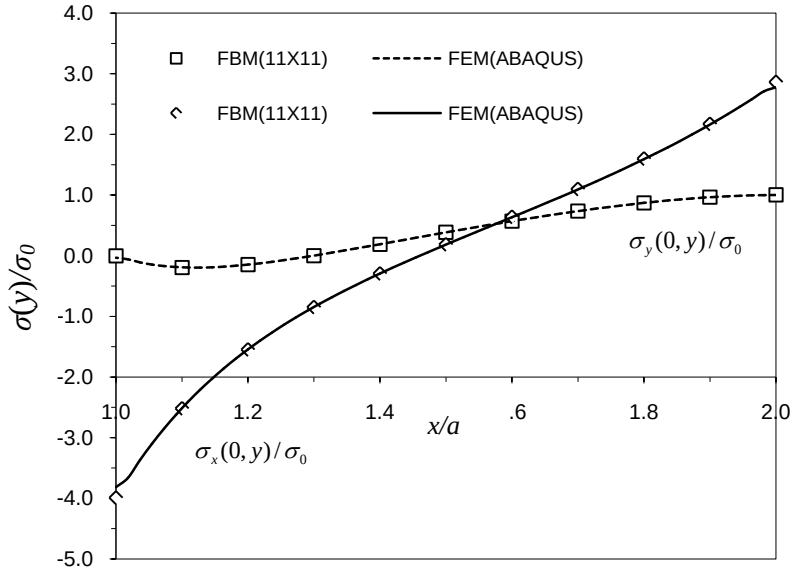

Figure 17. Normalized stresses along axis *y*.

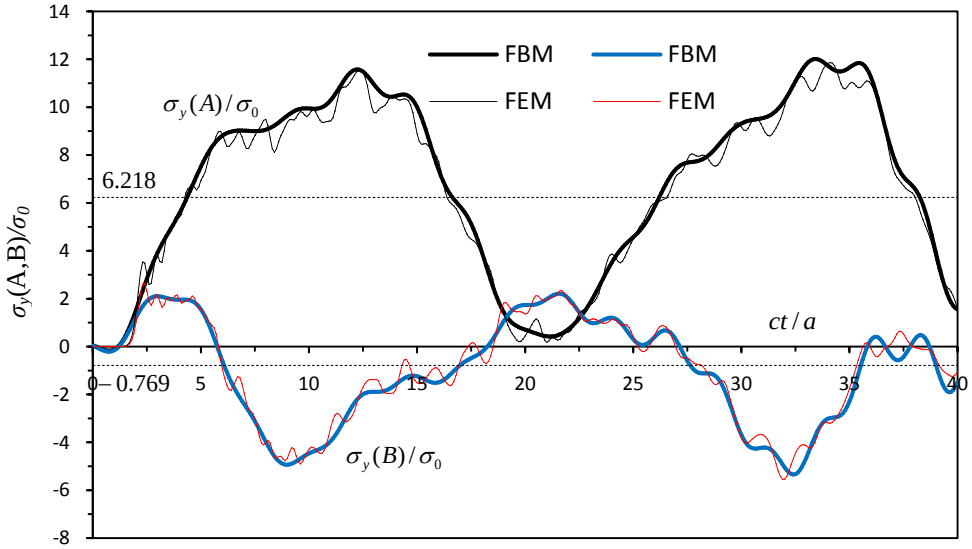

Figure 18. Normalized stresses $\sigma_y(t)/\sigma_0$ at locations A and B.

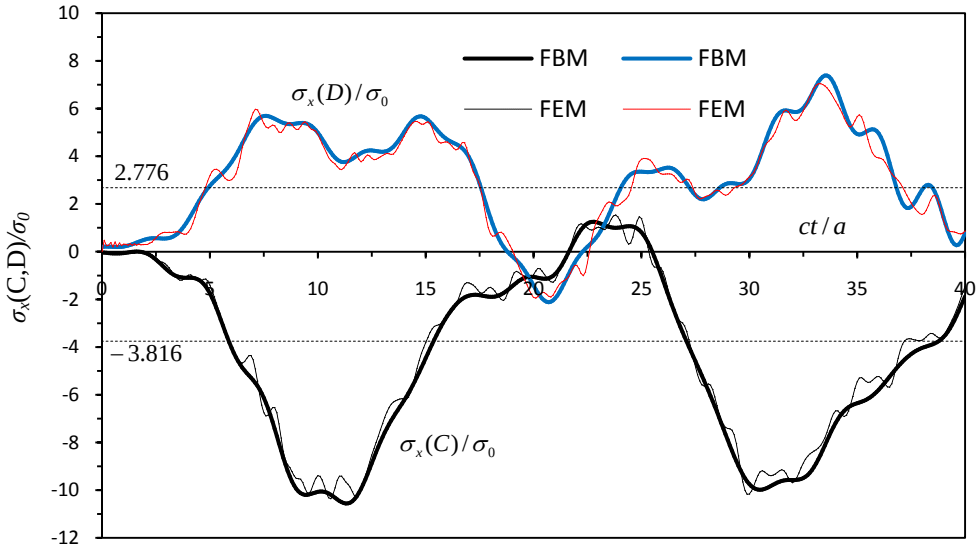

Figure 19. Normalized stresses $\sigma_x(t)/\sigma_0$ at locations C and D.

6. Conclusion

The boundary node Petrov-Galerkin method was developed to investigate two-dimensional elastic problems with functionally graded materials. The displacement of internal points can be obtained in terms of the outer boundary displacements from the governing equations in weak form. Therefore, stresses can be represented by the boundary displacements. The essential features of the proposed numerical techniques in this paper can be summarized as:

(1) The physical domain is divided into few blocks with quadratic elements (blocks);

(2) First order partial differential matrices $\mathbf{D}_x$ and $\mathbf{D}_y$ are easily obtained by the Lagrange series interpolation in terms of boundary displacements;

(3) BNPGM has characteristics of the boundary element method as the tractions can be expressed with boundary displacements;

(4) Functionally graded materials anisotropic media or all kind of boundary value problems of partial differential equations with variable coefficients can be analyzed easily;

In addition, the BNPGM can be extended easily to any types of partial differential, including Ressiener/Midllin plate bending, large deformation of plate bending and other nonlinear problems in engineering.

References

[1] Aliabadi MH. The Boundary Element, Applications in Solids and Structures, John Wiley and Sons, Ltd., Chichester, England, 2002.

[2] S.N. Atluri, The Meshless Method (MLPG) for Domain and BIE Discretizations, Forsyth, GA, USA, Tech Science Press, 2004.

[3] Liu GR. Meshfree Methods: Moving Beyond the Finite Element Method, Second Edition. CRC Press, 2009.

[4] Golberg MA, Chen CS. The method of fundamental solutions for potential, Helmholtz and diffusion problems. In: Golberg MA, editor. Boundary integral methods-numerical and mathematical aspects. Southampton, UK: Comput. Mech. Publ.; 1998. 103–76.

[5] Kythe PK. Fundamental solutions for differential operators and applications. Boston: Birkhauser; 1996.

[6] Cheng A. Particular solutions of Laplacian, Helmholtz-type, and polyharmonic operators involving higher order radial basis functions. Eng Anal Bound Elem 2000;24:531-538.

[7] Y.C. Hon, T. Wei. A fundamental solution method for inverse heat conduction problem. Engineering Analysis with Boundary Elements, 2004, 28(5):489-495.

[8] L. Lucy. A numerical approach to testing the fission hypothesis. Astron. J. 1977, 82:1013-1024.

[9] J.J. Monaghan. An introduction to SPH. Comput. Phyys. Commun., 1988, 48: 89-96.

[10] P.W. Randles, L.D. Libersky. Smoothed particle hypodynamics: some recent Improvements and application. Comput. Meth. Appl. Mech. Engng. 1996,139: 375-408.

[11] B.Nayroles, G. Touzot & P. Villon, Generalizing the finite element method: diffuse approximation and diffuse elements, Computational Mechanics, 10, 307-318, 1992.

[12] T. Belytschko, Y.Y. Lu & L. Gu, Element-free Galerkin method, Int. J. Numerical Methods in Engineering, 37, 229-256, 1994.

[13] Y.Y.Liu, T. Belytschko, L. Gu. A new implementation of the element free Galerkin method. Comput. Meth. Appl. Mech. Engng, 1994, 113: 397-414.

[14] T. Belytschko, M. Tabarra. Dynamic fracture using element free Galerkin methods. Int. J. Numerical Methods in Engineering, 1996, 39:923-938.

[15] S.N. Atluri & T. Zhu, A new meshless local Peyrov-Galerkin (MLPG) approach to nonlinear problems in computational modelling and simulation, Comput Model Simul Engng, 3, 187-196, 1998.

[16] S.N. Atluri & T. Zhu, The meshlesss local Peyrov-Galerkin (MLPG) approach for sovling problems in elasto-statics, Comput Mech, 25, 169-179, 1999.

[17] S.N. Atluri & S. Shen, The meshlesss local Peyrov-Galerkin (MLPG) method: a simple and less-costly alternative to the finite element and boundary element method, Comput Model Engng Sci, 3, 11-52, 2002.

[19] Sladek V., Sladek J., Zhang Ch. Local integro-differential equations with domain elements for the numerical solution of partial differential equations with variable coefficients, Journal of Engineering Mathematics 2005; 51: 261-282.

[20] V. Sladek, J. Sladek, M. Tanaka & Ch. Zhang, Local integral equation method for potential problems in functionally graded anisotropic materials, Engng Analy with Boundary Elements, 29, 829-843, 2005.

[21] J. Sladek, V. Sladek, P. Solek: Elastic analyses in 3D anisotropic functionally graded solids by the MLPG. CMES - Computer Modeling in Engineering & Sciences 43, 223-251, 2009.

[22] Wen PH, Cao P, Korakianitis T. Finite Block Method in elasticity. Engng Analysis with Boundary Elements 2014; 46: 116-125.

[23] Li M, Wen PH. Finite block method for transient heat conduction analysis in functionally graded media, Int. J. Numerical Methods in Engineering Int. J. Numer. Meth. Engng 2014; 99:372–390.

[24] Stehfest H. Algorithm 368: numerical inversion of Laplace transform. Comm. Assoc. Comput. Math,. 13: 47-49.

[25] Durbin F. Numerical inversion of Laplace transforms: an efficient improvement to Dubner and Abate's method. The Computer J. 1975; 17: 371-376.

[26] Wen PH, Aliabadi MH. An Improved Meshless Collocation Method for Elastostatic and Elastodynamic Problems. Journal Communications in Numerical Methods in Engineering 2008; 24 (8): 635-651.